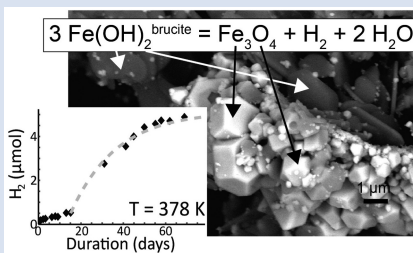# Kinetics of low-temperature H_2 production in ultramafic rocks by ferroan brucite oxidation

W. Carlin[1,2], B. Malvoisin[1]*, F. Brunet[1], B. Lanson[1], N. Findling[1], M. Lanson[1],
T. Fargetton[2], L. Jeannin[2], O. Lhote[2]

Abstract

Ferroan brucite, $(Mg,Fe)(OH)_2$, is among the potential mineral candidates for low temperature (<423 K) abiotic H_2 production in ultramafic rocks. To verify this assumption, synthetic ferroan brucite with grain size similar to that observed in natural samples (40–100 nm) was reacted with pure water at temperatures ranging from 348 to 573 K. Experimental products are consistent with the reaction $3 \ Fe(OH)_2^{brucite} = Fe_3O_4 + H_2 + 2 \ H_2O$. This reaction reached completion in ~2 months at 378 K and is thermally activated with an activation energy of 145 ± 1 kJ/mol. The standard state formation enthalpy and the third law entropy of amakinite, $Fe(OH)_2$, were refined from the experimental dataset. The new thermodynamic parameters imply that ferroan brucite is stable at significantly lower hydrogen activity than previously calculated. The alteration of Fe-brucite produces H_2 at rates compatible with present day observations of H_2 emissions in natural settings (ophiolite and mid-oceanic ridges). However, efficient fluid renewal is required, as opposed to H_2 production through olivine serpentinisation, which can proceed in static hydraulic conditions.

Introduction

Hydrothermal circulation across upper mantle rocks at mid-ocean ridges promotes serpentinisation reactions. In the course of these reactions, olivine reacts with water to form serpentine, magnetite and ferroan brucite, $(Mg,Fe)(OH)_2$, along with abiotic hydrogen (Moody, 1976). As observed in ophiolites (Neal and Stanger, 1983; Abrajano et al., 1990; Leong et al., 2023), ultramafic rocks can still produce H_2 at low temperature (i.e. at $T < 423$ K), even if they are extensively serpentinised. The extrapolation of experimental kinetic data collected in the 473–623 K range (e.g., McCollom et al., 2016) indicates that serpentinisation of olivine with a grain size of 500 µm should reach a reaction progress above 90 % in at least 10,000 yr at temperatures below 423 K.

The serpentinisation of olivine produces secondary minerals, including ferroan brucite, which are Fe^{2+}-rich and which can further react to produce H_2 + magnetite at low temperature:

$$3[Fe(OH)_2]^{brucite} = Fe_3O_4 + H_2 + 2H_2O \qquad Eq. 1$$
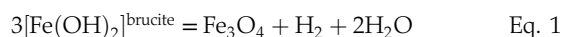
where $[Fe(OH)_2]^{brucite}$ represents the Fe component of ferroan brucite.

Petrographic data on ophiolite and dredge seafloor samples (Jöns et al., 2017; Klein et al., 2020; Ellison et al., 2021) seem to indicate that Reaction 1 could proceed at sub-surface conditions in partly serpentinised ultramafic rocks. H_2 production was achieved in hydrothermal experiments carried out

on serpentinised peridotite at 373 K and was attributed to magnetite formation at the expense of ferroan brucite (Miller et al., 2017).

In order to test the potential of Reaction 1 to produce H_2 at temperatures below 423 K in ultramafic rocks, the kinetics and thermodynamics of Reaction 1 were investigated experimentally here using synthetic $(Mg_{1-x}Fe_x)(OH)_2$ of grain size (40–100 nm) and composition (x from 0.156 to 0.205) relevant to natural ferroan brucite (Malvoisin et al., 2020).

Materials and Methods

Ferroan brucite $(Mg_{1-x}Fe_x)(OH)_2$, with x ranging from 0.156 to 0.205, was synthesised under ambient conditions from a stoichiometric solution of dissolved Fe(II) and Mg chlorides, as described in Carlin et al. (2023). The ferroan brucite obtained by this method formed platelets 40 to 100 nm across (Fig. 1a). It was loaded under an Ar atmosphere with degassed ultrapure water either in welded shut gold capsules ('caps' experiments) or in 50 mL Parr 5500 series titanium reactors ('SP' experiments; see details in Tables S-2 and S-3). The capsules were run either in horizontal cold seal pressure vessels at temperatures from 348 to 573 K at 20 MPa (caps#1 to #15) or in an oven at temperatures of 378 and 423 K at the liquid-vapour equilibrium pressure (P_{sat}, caps#t1 to #t12). Titanium reactor experiments, SP#3 to SP#5, were conducted in the 423 to 473 K range, also at P_{sat}. SP#6 was run at 378 K with an initial Ar pressure of ~5 MPa.

1. Université Grenoble Alpes, USMB, CNRS, IRD, UGE, ISTerre, France
2. Storengy, ENGIE, France
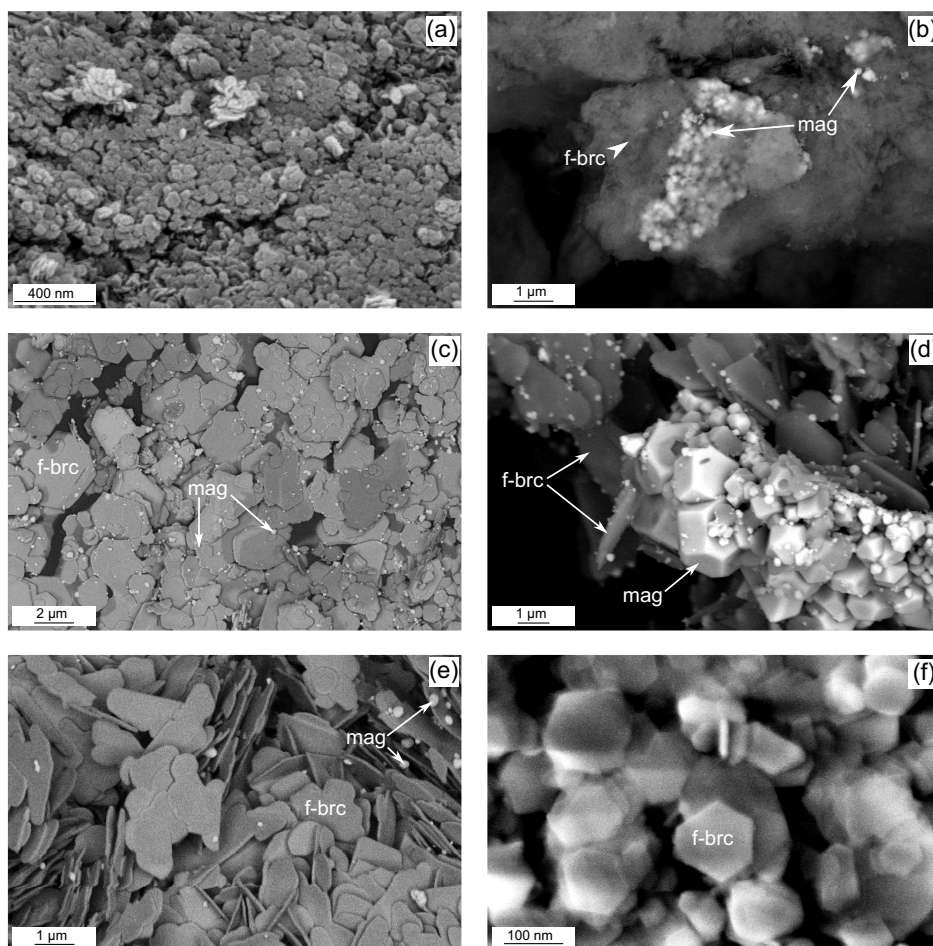* Corresponding author (email: benjamin.malvoisin@univ-grenoble-alpes.fr)

Figure 1 Back-scattered images of **(a)** the starting ferroan brucite and **(b–f)** its reaction products. **(b)** Caps#9; 378 K, 2.5 days. **(c, d)** SP#3; 473 K, 8 days. Euhedral micrometre-sized magnetite is visible. **(e)** Caps#15; 573 K, 2 days. Note that ferroan brucite platelets have recrystallised. **(f)** SP#6; 378 K, 69 days. ~100 nm wide euhedral ferroan brucite platelets are observed. f-brc, ferroan brucite; mag, magnetite.

Pressure evolution in SP experiments was monitored at ±2 kPa with a Keller pressure sensor PA-33X. After the experiments, the H_2 produced and trapped in the gold capsule was sampled using the protocol described in Malvoisin *et al.* (2013) and analysed by gas chromatography. H_2 leakage through the gold capsule walls is negligible at the temperatures investigated here (Malvoisin *et al.*, 2013). The amount of H_2 produced in titanium reactors was quantified either on the gas sampled at the run conditions, and/or at the end of the experiment. No H_2 was detected in two blank experiments performed at 378 and 473 K over more than 40 days with capsules containing only degassed ultrapure water (100 μL). Before experiments, the titanium reactors were heated to 523 K during one day in air to extract any H_2 potentially solubilised in the reactor wall (Louthan and Derrick, 1975), and to ensure Ti surface oxidation prior to reaction. No hydrogen production was detected in these blank experiments. Details of the sample characterisation techniques are provided in the Supplementary Information.

Results and Discussion

Ferroan brucite oxidation reaction. In all experiments, ferroan brucite partly decomposed into magnetite + H_2 (Table S-2). The H_2 yield increased from 4×10^{-3} to 220 μmol of H_2 *per* gram of starting material when the temperature increased from 348 to 573 K. In eight experiments (Table S-2), pyroaurite was detected (<20 wt. %), indicating the presence of minor CO_2 in the reacting medium. Pyroaurite does not involve significant H_2 production (Carlin *et al.*, 2023). Its impact on H_2 production rate is, thus, mainly associated with the lowering of the amount of ferroan brucite available for H_2 production. However, for experiments used for determining kinetic and thermodynamic parameters, we estimated that a maximum of 3.4 wt. % of the initial ferroan brucite was consumed to form pyroaurite. This leads to an error on the H_2 production rate that is small compared to the error associated with H_2 measurement of ~11 %. The Fe content ($X_{Fe(OH)_2}$) of ferroan brucite was determined from the refined unit cell parameters (Table S-2) based on Vegard's law (Carlin *et al.*, 2023). It was found to vary from 0.1 to 0.2, *i.e.* equal or slightly below $X_{Fe(OH)_2}$ in the ferroan brucite starting material. Recrystallisation of ferroan brucite as platelets was observed in the highest temperature experiments (Fig. 1). Unless metastable growth occurred, this observation suggests that ferroan brucite with $X_{Fe(OH)_2} < 0.2$ is a stable reaction product in these experiments.

Altogether, the experimental results revealed that brucite partly reacted during the experiments according to Reaction 1, leading to the overall reaction:

$$(1 - x + y)Mg_{(1-x)}Fe_x(OH)_2 = (1 - x)Mg_{(1-x+y)}Fe_{(x-y)}(OH)_2$$

$$+ \frac{y}{3}Fe_3O_4 + \frac{2y}{3}H_2O + \frac{y}{3}H_2$$
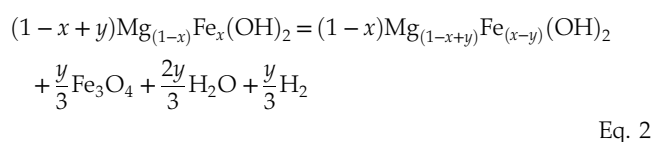
Eq. 2

where x is the initial $X_{\mathrm{Fe(OH)_2}}$ and y is a parameter related to reaction progress such as $0 \leq y \leq x$, which reflects that only a fraction, y/x, of the $Fe(OH)_2$ component in ferroan brucite has reacted. Indeed, thermodynamic equilibrium may well be achieved for $y < x$.

H_2 production rate and brucite oxidation rate. The amount of produced H_2 was used to retrieve the progress of Reaction 2. Magnetite was not used to infer reaction progress because, due to the presence of minor Fe^{3+} in the starting material, part of the magnetite product may form independently of Reaction 2, *i.e.* without H_2 production (Carlin *et al.*, 2023). The amount of H_2 produced in the SP experiments did not induce pressure changes significant enough to retrieve isothermal H_2-production rate laws directly from pressure monitoring. However, the qualitative pressure evolution was used to determine the overall duration of the H_2 production stage, which, in turn, was used to model the reaction kinetics (see Supplementary Information for details). H_2 production kinetics at 378 K could be accurately retrieved from Run SP#6, where gas was regularly sampled (Fig. 2a). In addition, a series of experiments in gold capsules (caps#t5 to #t12) were stopped after different durations and H_2 was analysed in order to further constrain the kinetics of Reaction 2 (Fig. 2b). These experimental data were fitted to a kinetic law (Lasaga, 1998; see Supplementary Information for details) with the reaction rate (r) as:

$$r = r_0 \times \left(1 - \frac{Q}{K}\right) \qquad \text{Eq. 3}$$

where $r_0 = k_0 \times A \times \exp\left(\frac{-E_a}{RT}\right)$ with k_0 a kinetic constant, A the $Fe(OH)_2$ specific surface area, E_a the activation energy, R the gas constant and T the temperature. Q and K are the reaction quotient and the equilibrium constant of Reaction 1, respectively. The standard state is defined here with unit activity for pure minerals and water at any temperature and pressure, as well as unit fugacity for ideal gas at 1 bar of pressure and any temperature. Q was approximated to $\frac{P_{\mathrm{H_2}}}{X_{\mathrm{Fe(OH)_2}}^3}$ with $P_{\mathrm{H_2}}$ the H_2 partial pressure at the conditions of the experiment and $X_{\mathrm{Fe(OH)_2}}$ the molar fraction of $Fe(OH)_2$ in ferroan brucite, by assuming ideal behaviour for H_2 and $Fe(OH)_2$ in the gas phase and in the brucite solid-solution, respectively. $X_{\mathrm{Fe(OH)_2}}$ was calculated from Equation 2, based on the number of moles of produced H_2 ($n_{\mathrm{H_2}}$). $P_{\mathrm{H_2}}$ was derived from $n_{\mathrm{H_2}}$ considering the amount of H_2 dissolved in the solution as calculated using PHREEQC (Parkhurst and Appelo, 2013). K was estimated with the same procedure as Q, by considering that equilibrium H_2 pressure equals the H_2 partial pressure in the gas at the last measurement multiplied by a factor, λ, slightly above 1 (see Supplementary Information for details on this factor). Fitted r_0 values are displayed in Figure 2c as a function of reciprocal temperature. The slope in the linear fit corresponds to an activation energy of 145 ± 1 kJ/mol. The intercept of the fit provides a $k_0 \times A$ quotient of 8.97×10^7 mol s^{-1} g^{-1}.

Experimental constraints on thermodynamic properties of ferroan brucite. Based on the kinetic law derived in the previous section, 17 experiments reached equilibrium (Table S-2). These experiments were, thus, used to constrain the equilibrium constant (K) of Reaction 1.

As discussed above, a set of K values can be calculated based on $n_{\mathrm{H_2}}$, measured at the end of each experiment. A pair of $\Delta_f H°$ and $S°$ values for the $Fe(OH)_2$ end member was retrieved by least square regression through this set of K values (see Supplementary Information for thermodynamic calculation details). $\Delta_f H°_{\mathrm{Fe(OH)_2}}$ and $S°_{\mathrm{Fe(OH)_2}}$ of -581.3 ± 2.9 kJ/mol and
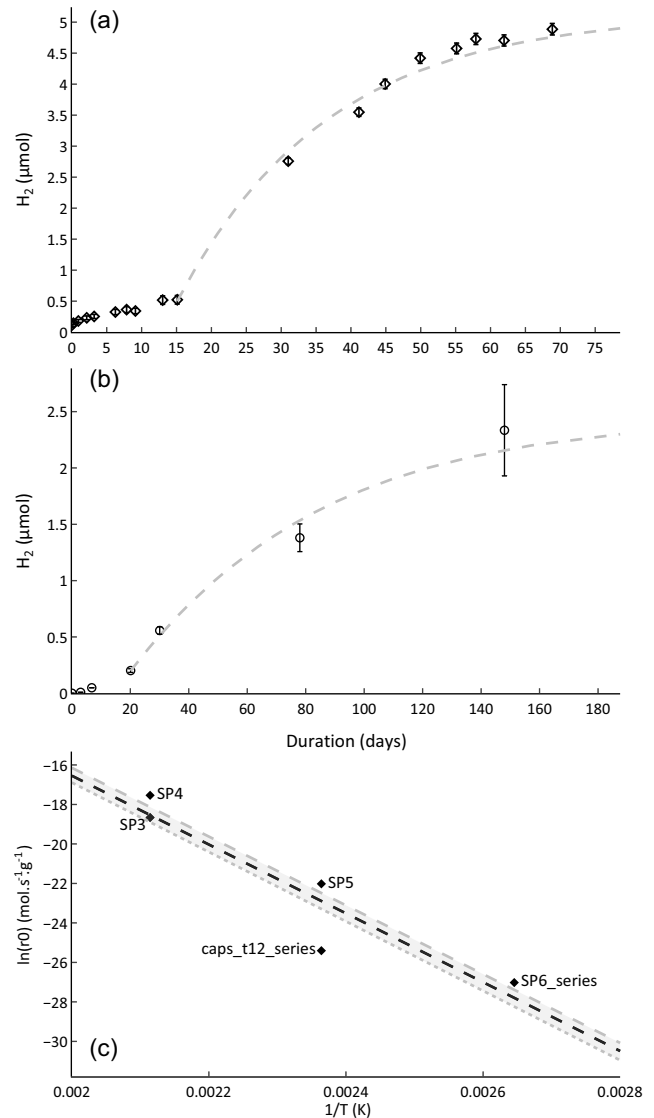
Figure 2 Kinetics of ferroan brucite alteration. **(a)** Number of moles of produced H_2 as a function of time at 378 K (Run SP#6; black diamonds). **(b)** Number of moles of produced H_2 as a function of time at 423 K (Runs caps#t5 to caps#t12; black circles). The dashed lines in **(a)** and **(b)** correspond to a fit of the data with Equation 3. **(c)** $\ln(r_0)$ *vs.* $1/T$. The linear regression of r_0 is displayed with a black dashed line ($R^2 = 0.87$) and the grey dashed lines are linear regressions for r_0 with λ values of 1.01 and 1.20.

86.4 ± 6.3 J/mol/K were obtained, respectively. These thermodynamic values are only relevant for calculations using the same standard states as those used here, as well as the same assumption of unit activity and fugacity coefficients for ferroan brucite solid solution and H_2 in the gas phase, respectively. They fall in the range of published values for $Fe(OH)_2$ (Table S-4, Fig. S-3). The $\Delta_f H°_{\mathrm{Fe(OH)_2}}$ value is consistent with the value by Ziemniak *et al.* (1995) and departs by 1.2 % from $\Delta_f H°_{\mathrm{Fe(OH)_2}}$, tabulated in the NIST-JANAF database (Chase, 1998). The values of the NIST-JANAF database only differ by 0.1 % from those commonly used for thermodynamic modelling of fluid–rock interactions in ultramafic rocks (McCollom and Bach, 2009). H_2 production prediction for our experiments is overestimated by more than one order of magnitude with the McCollom and Bach's (2009) database (Fig. S-4).

Implications for low-T H_2 production in ultramafic systems. Olivine serpentinisation (*e.g.*, McCollom *et al.*, 2016)
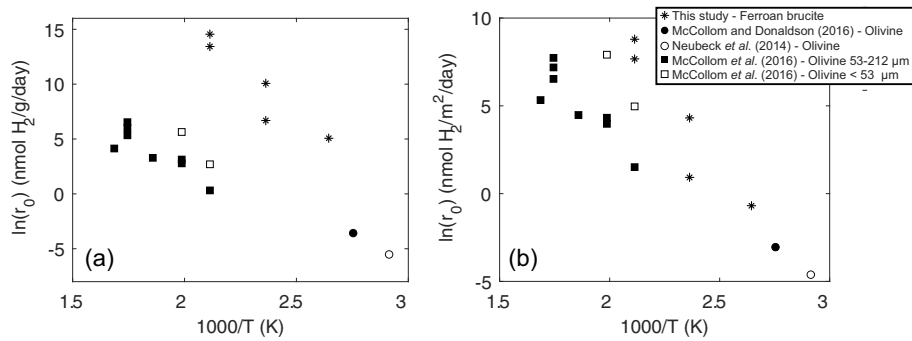
Figure 3 Comparison of experimentally determined rate of H_2 production for ferroan brucite (r_0, this study) and olivine serpentinisation (Neubeck *et al.*, 2014; McCollom and Donaldson, 2016; McCollom *et al.*, 2016). **(a)** Reaction rate *per* mass of starting material (r_0). **(b)** Reaction rate *per* reactive surface area (r_0/A) with A the specific surface area either measured with the BET method or calculated with the relationship provided in Brantley and Mellott (2000).

and ferroan brucite alteration (Miller *et al.*, 2017; Ellison *et al.*, 2021) are the two main processes that have been proposed to account for H_2 production at low temperature ($T < 423\,K$) in ultramafic rocks. Excluding kinetic experiments interpreted as being distorted by artefacts (McCollom and Donaldson, 2016), a maximum of 0.028 nmol H_2/g olivine/day was proposed for H_2 production by olivine serpentinisation at 363 K (Fig. 3a). In comparison, the rate of H_2 production measured here during ferroan brucite reaction (r_0) is approximately three orders of magnitude higher (Fig. 3a). When weighted by the specific surface area of the powders used in the various experiments, however, the reaction rates are rather well aligned in an Arrhenius plot with an activation energy of ~81 kJ/mol (Fig. 3b). The difference in grain sizes between olivine used in the experiments depicted in Figure 3 (38–212 μm) and the synthetic ferroan brucite used here (~50 nm) probably plays a key role in their difference of reactivity.

The respective contribution of olivine and Fe-brucite alteration to the H_2 production rate in natural systems was evaluated using a numerical approach. A fluid–serpentinised dunite system composed of olivine (grain size of 500 μm; Malvoisin *et al.*, 2017), ferroan brucite (grain size of 50 nm; Malvoisin *et al.*, 2021) and water was modelled with H_2 being only produced by alteration of the latter minerals. A range of escape rates of H_2 (advection and/or diffusion) was defined in order to simulate hydrothermal activity at mid-ocean ridges, water infiltration in an ophiolitic unit or sub-stagnant hydraulic conditions in a deep aquifer. The temperature was set to 363 K, relevant to low-T serpentinisation (Fig. 4; see model details in Supplementary Information).

The model shows that ferroan brucite is the first mineral to react with a rate that is three orders of magnitude faster than that of olivine, leading to a rapid H_2 production in the first year of the reaction (Fig. 4b). In a closed system, ferroan brucite reaction rapidly stops due to the attainment of thermodynamic equilibrium ($Q/K = 1$). The adjustment of the thermodynamic parameters of $Fe(OH)_2$ proposed here (1.8 % and 1.2 % for $S^\circ_{Fe(OH)_2}$ and $\Delta_f H^\circ_{Fe(OH)_2}$, respectively, compared to the database of McCollom and Bach, 2009) has a strong impact on the predicted equilibrium H_2 partial pressure and, thus, on the amount of H_2 that is produced. At 363 K, equilibrium is achieved for a H_2 molality of 2.2×10^{-5} mol/kg, while it is two orders of magnitude higher (5.0×10^{-3} mol/kg) with the database of McCollom and Bach (2009). At 313 K, a difference of three orders of magnitude for H_2 molality between the two database is predicted. The oxygen fugacity (fO_2) lies on the $H_2O/H_2(g)$ equilibrium with the database of McCollom and Bach (2009) and five orders of magnitude above with the thermodynamic data derived here. Interestingly, this latter fO_2 is consistent with the fO_2 measured at the bottom of Holes BA1A, BA1D and BA4A during the Oman Drilling Project (Kelemen *et al.*, 2021). After ferroan brucite reaction, olivine completely reacts in the model in approximately 3 Myr and ultimately produces 3000 times more H_2 than ferroan brucite (Fig. 4a).

Ferroan brucite can further react if, at the same time, H_2 escapes from the system at a rate exceeding that of H_2 production associated with olivine serpentinisation (Fig. 4c). This corresponds to minimum H_2 escape rates of 10^{-5} and 7×10^{-4} mol H_2/day/g rock at 313 and 363 K, respectively. The estimated
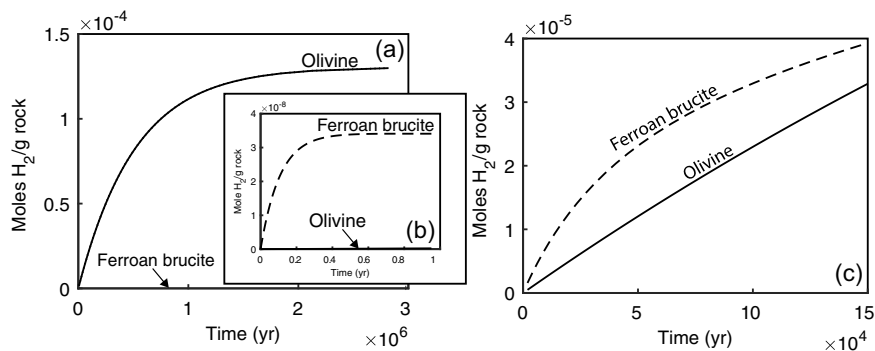

Figure 4 Numerical modelling of the contribution of ferroan brucite alteration and olivine serpentinisation to H_2 production as a function of time in a partly altered peridotite (see Supplementary Information for details). **(a)** General view and **(b)** incipient stage simulation in a closed system (no H_2 leak associated with diffusion or fluid advection). **(c)** Simulation by considering advection of a fluid at a rate of 1.4×10^{-4} kg water/day/kg rock. Dashed line: H_2 production associated with ferroan brucite alteration. Solid line: H_2 production associated with olivine serpentinisation.

maximum escape rate by vertical diffusion is three orders of magnitude lower than this threshold value (see Supplementary Information for details), suggesting that vertical diffusion is not sufficient to drive ferran brucite reaction. The threshold value is achieved by water renewal at a minimum rate of 7×10^{-6} and 3×10^{-5} kg water/day/kg rock at 313 and 363 K, respectively. The average water-to-rock ratio at mid-ocean ridges is ~1 (Coogan *et al.*, 2019). Considering hydrothermal activity and fluid flow during a minimum of 30,000 yr (Früh-Green *et al.*, 2003), it can be converted into a mean water flux of 10^{-7} kg water/day/kg rock. In the Oman ophiolite, ferran brucite with $x = 0.28$ can represent ~50 mol % of the serpentinisation reaction products (Malvoisin *et al.*, 2020). Present day alteration of such ferran brucite may occur during interaction with rainwater. H_2-rich hyperalkaline fluids are found at depths >50 m (Leong *et al.*, 2023), and the recharge rate of the aquifer in Oman is 18 mm/year (Dewandel *et al.*, 2005). Combining these values leads to a mean meteoritic water flux of 3×10^{-7} kg water/day/kg rock. Both in ophiolites and on the seafloor, mean water flux estimates are, thus, approximately one order of magnitude lower than the minimum flux necessary to drive ferran brucite reaction. However, fluid flow in ultramafic rocks is concentrated in cracks and microcracks (Dewandel *et al.*, 2005; Corre *et al.*, 2023) and is, thus, expected to be, locally, several orders of magnitude higher than the mean water flux. For example, the highest water-to-rock ratio values reported in abyssal peridotites are above 10^5 (Snow and Reisberg, 1995; Delacour *et al.*, 2008), corresponding to water fluxes >10^{-2} kg water/day/kg rock compatible with H_2 production associated with ferran brucite oxidation. The measured maximum H_2 production rate in the Oman ophiolite is of 71,000 mol H_2/yr for a minimal volume of altered rock of 0.05 km^3 (Leong *et al.*, 2023). This corresponds to a specific flux of 10^{-3} nmol H_2/g rock/day which is consistent with the specific H_2 production rate of 5×10^{-3} nmol H_2/g rock/day, estimated at 313 K based on the extrapolation of the data acquired here for ferran brucite alteration (Fig. 3). Actually, the same extrapolation for serpentinisation of olivine having a grain size of 500 µm (Fig. 3b) yields a much lower production rate of 10^{-5} nmol H_2/g rock/day at 313 K. Ferran brucite oxidation could thus be a main contributor to H_2 production at temperatures below 423 K in ophiolites and on the seafloor. This is consistent with petrographic observations in natural samples showing ferran brucite oxidation to form magnetite in open systems conditions (Bach *et al.*, 2006; Jöns *et al.*, 2017).

Acknowledgements

Additional Information

References

ABRAJANO, T.A., STURCHIO, N.C., KENNEDY, B.M., LYON, G.L., MUEHLENBACHS, K., BOHLKE, J.K. (1990) Geochemistry of reduced gas related to serpentinization of the Zambales ophiolite, Philippines. *Applied Geochemistry* 5, 625–630. https://doi.org/10.1016/0883-2927(90)90060-I

BACH, W., PAULICK, H., GARRIDO, C.J., ILDEFONSE, B., MEURER, W.P., HUMPHRIS, S.E. (2006) Unraveling the sequence of serpentinization reactions: petrography, mineral chemistry, and petrophysics of serpentinites from MAR 15°N (ODP Leg 209, Site 1274). *Geophysical Research Letters* 33, L13306. https://doi.org/10.1029/2006GL025681

BRANTLEY, S.L., MELLOTT, N.P. (2000) Surface area and porosity of primary silicate minerals. *American Mineralogist* 8, 1767–1783. https://doi.org/10.2138/am-2000-11-1220

CARLIN, W., MALVOISIN, B., LANSON, B., BRUNET, F., FINDLING, N., LANSON, M., MAGNIN, V., FARGETTON, T., JEANNIN, L., LHOTE, O. (2023) Fe^{III}-substituted brucite: Hydrothermal synthesis from (Mg$_{0.8}$Fe$^{II}_{0.2}$)-brucite, crystal chemistry and relevance to the alteration of ultramafic rocks. *Applied Clay Science* 234, 106845. https://doi.org/10.1016/j.clay.2023.106845

CHASE, M.W. (1998) *NIST-JANAF Thermochemical Tables*. Fourth Edition, American Chemical Society, Washington, D.C.

COOGAN, L.A., SEYFRIED, W.E., PESTER, N.J. (2019) Environmental controls on mid-ocean ridge hydrothermal fluxes. *Chemical Geology* 528, 119285. https://doi.org/10.1016/j.chemgeo.2019.119285

CORRE, M., BRUNET, F., SCHWARTZ, S., GAUTHERON, C., AGRANIER, A., LESIMPLE, S. (2023) Quaternary low-temperature serpentinization and carbonation in the New Caledonia ophiolite. *Scientific Reports* 13, 19413. https://doi.org/10.1038/s41598-023-46691-y

DELACOUR, A., FRÜH-GREEN, G.L., FRANK, M., GUTJAHR, M., KELLEY, D.S. (2008) Sr- and Nd-isotope geochemistry of the Atlantis Massif (30°N, MAR): Implications for fluid fluxes and lithospheric heterogeneity. *Chemical Geology* 254, 19–35. https://doi.org/10.1016/j.chemgeo.2008.05.018

DEWANDEL, B., LACHASSAGNE, P., BOUDIER, F., AL-HATTALI, S., LADOUCHE, B., PINAULT, J.-L., AL-SULEIMANI, Z. (2005) A conceptual hydrogeological model of ophiolite hard-rock aquifers in Oman based on a multiscale and a multidisciplinary approach. *Hydrogeology Journal* 13, 708–726. https://doi.org/10.1007/s10040-005-0449-2

ELLISON, E.T., TEMPLETON, A.S., ZEIGLER, S.D., MAYHEW, L.E., KELEMEN, P.B., MATTER, J.M., The Oman Drilling Project Science Party (2021) Low-Temperature Hydrogen Formation During Aqueous Alteration of Serpentinized Peridotite in the Samail Ophiolite. *Journal of Geophysical Research: Solid Earth* 126, e2021JB021981. https://doi.org/10.1029/2021JB021981

FRÜH-GREEN, G.L., KELLEY, D.S., BERNASCONI, S.M., KARSON, J.A., LUDWIG, K.A., BUTTERFIELD, D.A., BOSCHI, C., PROSKUROWSKI, G. (2003) 30,000 Years of Hydrothermal Activity at the Lost City Vent Field. *Science* 301, 495–498. https://doi.org/10.1126/science.1085582

JÖNS, N., KAHL, W.-A., BACH, W. (2017) Reaction-induced porosity and onset of low-temperature carbonation in abyssal peridotites: Insights from 3D high-resolution microtomography. *Lithos* 268–271, 274–284. https://doi.org/10.1016/j.lithos.2016.11.014

KELEMEN, P.B., LEONG, J.A., DE OBESO, J.C., MATTER, J.M., ELLISON, E.T., TEMPLETON, A., NOTHAFT, D.B., ESLAMI, A., EVANS, K., GODARD, M., MALVOISIN, B., COGGON, J.A., WARSI, N.H., PÉZARD, P., CHOE, S., TEAGLE, D.A.H., MICHIBAYASHI, K., TAKAZAWA, E., AL SULAIMANI, Z., The Oman Drilling Project Science Team (2021) Initial Results From the Oman Drilling Project Multi-Borehole Observatory: Petrogenesis and Ongoing Alteration of Mantle Peridotite in the Weathering Horizon. *Journal of Geophysical Research: Solid Earth* 126, e2021JB022729. https://doi.org/10.1029/2021JB022729

KLEIN, F., HUMPHRIS, S.E., BACH, W. (2020) Brucite formation and dissolution in oceanic serpentinite. *Geochemical Perspectives Letters* 16, 1–5. https://doi.org/10.7185/geochemlet.2035

LASAGA, A.C. (1998) *Kinetic Theory in the Earth Sciences.* Princeton University Press, Princeton, NJ.

LEONG, J.A., NIELSEN, M., MCQUEEN, N., KAROLYTÉ, R., HILLEGONDS, D.J., BALLENTINE, C., DARRAH, T., MCGILLIS, W., KELEMEN, P. (2023) H_2 and CH_4 outgassing rates in the Samail ophiolite, Oman: Implications for low-temperature, continental serpentinization rates. *Geochimica et Cosmochimica Acta* 347, 1–15. https://doi.org/10.1016/j.gca.2023.02.008

LOUTHAN JR., M.R., DERRICK, R.G. (1975) Hydrogen transport in austenitic stainless steel. *Corrosion Science* 15, 565–577. https://doi.org/10.1016/0010-938X(75)90022-0

MALVOISIN, B., BRUNET, F., CARLUT, J., MONTES-HERNANDEZ, G., FINDLING, N., LANSON, M., VIDAL, O., BOTTERO, J.-Y., GOFFÉ, B. (2013) High-purity hydrogen gas from the reaction between BOF steel slag and water in the 473–673 K range. *International Journal of Hydrogen Energy* 38, 7382–7393. https://doi.org/10.1016/j.ijhydene.2013.03.163

MALVOISIN, B., BRANTUT, N., KACZMAREK, M.-A. (2017) Control of serpentinisation rate by reaction-induced cracking. *Earth and Planetary Science Letters* 476, 143–152. https://doi.org/10.1016/j.epsl.2017.07.042

MALVOISIN, B., ZHANG, C., MÜNTENER, O., BAUMGARTNER, L.P., KELEMEN, P.B., Oman Drilling Project Science Party (2020) Measurement of Volume Change and Mass Transfer During Serpentinization: Insights From the Oman Drilling Project. *Journal of Geophysical Research: Solid Earth* 125, e2019JB018877. https://doi.org/10.1029/2019JB018877

MALVOISIN, B., AUZENDE, A.-L., KELEMEN, P.B., the Oman Drilling Project Science Party (2021) Nanostructure of serpentinisation products: Importance for water transport and low-temperature alteration. *Earth and Planetary Science Letters* 576, 117212. https://doi.org/10.1016/j.epsl.2021.117212

MCCOLLOM, T.M., BACH, W. (2009) Thermodynamic constraints on hydrogen generation during serpentinization of ultramafic rocks. *Geochimica et Cosmochimica Acta* 73, 856–875. https://doi.org/10.1016/j.gca.2008.10.032

MCCOLLOM, T.M., DONALDSON, C. (2016) Generation of Hydrogen and Methane during Experimental Low-Temperature Reaction of Ultramafic Rocks with Water. *Astrobiology* 16, 389–406. https://doi.org/10.1089/ast.2015.1382

MCCOLLOM, T.M., KLEIN, F., ROBBINS, M., MOSKOWITZ, B., BERQUÓ, T.S., JÖNS, N., BACH, W., TEMPLETON, A. (2016) Temperature trends for reaction rates, hydrogen generation, and partitioning of iron during experimental serpentinization of olivine. *Geochimica et Cosmochimica Acta* 181, 175–200. https://doi.org/10.1016/j.gca.2016.03.002

MILLER, H.M., MAYHEW, L.E., ELLISON, E.T., KELEMEN, P., KUBO, M., TEMPLETON, A.S. (2017) Low temperature hydrogen production during experimental hydration of partially-serpentinized dunite. *Geochimica et Cosmochimica Acta* 209, 161–183. https://doi.org/10.1016/j.gca.2017.04.022

MOODY, J.B. (1976) Serpentinization: a review. *Lithos* 9, 125–138. https://doi.org/10.1016/0024-4937(76)90030-X

NEAL, C., STANGER, G. (1983) Hydrogen generation from mantle source rocks in Oman. *Earth and Planetary Science Letters* 66, 315–320. https://doi.org/10.1016/0012-821X(83)90144-9

NEUBECK, A., DUC, N.T., HELLEVANG, H., OZE, C., BASTVIKEN, D., BACSIK, Z., HOLM, N.G. (2014) Olivine alteration and H_2 production in carbonate-rich, low temperature aqueous environments. *Planetary and Space Science* 96, 51–61. https://doi.org/10.1016/j.pss.2014.02.014

PARKHURST, D.L., APPELO, C.A.J. (2013) *Description of Input and Examples for PHREEQC Version 3—A Computer Program for Speciation, Batch-Reaction, One-Dimensional Transport, and Inverse Geochemical Calculations.* USGS Techniques and Methods 6–A43, U.S. Geological Survey, Denver, CO. https://pubs.usgs.gov/tm/06/a43/

SNOW, J.E., REISBERG, L. (1995) Os isotopic systematics of the MORB mantle: results from altered abyssal peridotites. *Earth and Planetary Science Letters* 133, 411–421. https://doi.org/10.1016/0012-821X(95)00099-X

ZIEMNIAK, S.E., JONES, M.E., COMBS, K.E.S. (1995) Magnetite solubility and phase stability in alkaline media at elevated temperatures. *Journal of Solution Chemistry* 24, 837–877. https://doi.org/10.1007/BF00973442

Kinetics of low-temperature H_2 production in ultramafic rocks by ferroan brucite oxidation

W. Carlin, B. Malvoisin, F. Brunet, B. Lanson, N. Findling,
M. Lanson, T. Fargetton, L. Jeannin, O. Lhote

Supplementary Information

The Supplementary Information includes:

- ➢ Characterisation Techniques
- ➢ Time Needed to Reach Thermodynamic Equilibrium in Titanium Reactors
- ➢ H_2 Production Rate-law
- ➢ Retrieval of $\Delta_f H°$ and $S°$ of the $Fe(OH)_2$ End Member: Calculation Method
- ➢ Numerical Modelling of H_2 Production During Serpentinised Dunite Alteration
- ➢ Tables S-1 to S-4
- ➢ Figures S-1 and S-4
- ➢ Supplementary Information References

An overview of the notation used throughout is given in Table S-1.

Characterisation Techniques

Gas phase contained in the sealed gold capsules was recovered after the experiments using the method described in Malvoisin *et al.* (2013). For titanium reactors, the gas phase was sampled in a syringe connected to the reactor headspace through a valve. For the gas analysis, 250 µL of gas was injected with gas-tight syringe in a Clarus 500 gas chromatograph (Perkin Elmer^{TM}) equipped with a polymer filled column (Restek ShinCarbon^{TM}) and a thermal conductivity detector (TCD). Argon was used as carrier gas. Each gas sample was analysed at least three times to check reproducibility. Based on these repeated measurements, the uncertainty on H_2 measurement is estimated to be ~11 % of the measured values (one standard deviation).

The recovered sample powder was characterised by X-ray diffraction (XRD) with a Bruker D8 diffractometer. XRD patterns were collected from 10 to 80° (2θ) using CuKα or CoKα radiation and counting times of 3 s per 0.04° step (Fig. S-1). XRD patterns were analysed using the Rietveld technique with the BGMN software (Doebelin and Kleeberg, 2015). Details of both the refinement strategy and refinement constraints are given in Carlin *et al.* (2023). The results of gas analyses and Rietveld refinement are provided in Tables S-2 and S-3.

Sample powders were mounted on double-sided carbon tape in the glove box for scanning electron microscopy (SEM) imaging. They were then coated under vacuum with a 1 nm thick gold layer and characterised with a field emission gun scanning electron microscope (FEG-SEM; Zeiss Ultra 55) operated at 5 to 10 kV.

Time Needed to Reach Thermodynamic Equilibrium in Titanium Reactors

Pressure evolution in SP experiments was monitored *in situ* (Fig. S-2). The hydrogen partial pressure, P_{H_2}, and thus the amount of produced H_2, n_{H_2}, were not retrieved from the *in situ* pressure monitoring. Indeed, as illustrated in Figure S-2, a steady state regime is achieved after an initial step of pressure increase but the steady-state pressure cannot be precisely retrieved due to a noise amplitude of ~30 kPa in the measured pressure. These variations have actually the same amplitude as the pressure increase generated by the reaction itself. For example, in experiment SP#5, the pressure oscillation (0.41–0.37 MPa) is equal to 40 kPa, *i.e.* close to the pressure increase generated by the complete reaction (Fig. S-2).

The *in situ* pressure monitoring could however be used to constrain the kinetics of ferroan brucite oxidation by retrieving the approximate reaction time needed to reach steady-state pressure conditions, even though the exact steady-state pressure could not be accurately determined. Steady-state pressure was assumed to represent near equilibrium conditions, and the corresponding reaction time was determined graphically for each SP experiments (Fig. S-2).

H$_2$ Production Rate-law

In the experiments conducted in gold capsules at ~20 MPa, no gas phase is present and H_2 occurs as an aqueous phase only:

$$3[Fe(OH)_2]^{brucite} = Fe_3O_4 + H_{2,aq} + 2H_2O. \qquad (S\text{-}1)$$
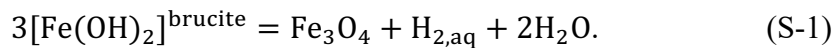
In the other experiments conducted on the liquid/vapour equilibrium, H_2 can be present as a gas phase:

$$3[Fe(OH)_2]^{brucite} = Fe_3O_4 + H_{2,g} + 2H_2O. \qquad (S\text{-}2)$$
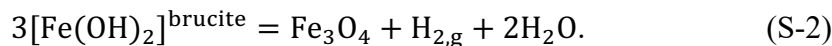
We assumed in the following that the kinetics of Reactions S-1 and S-2 are the same. This implies that H_2 transfer between the aqueous and the gaseous phases is not a rate-limiting step (*i.e.* rapid compared to the other processes involved in the reaction). Under this assumption, hydrogen production rate (*r*) according to Reactions S-1 and S-2 can be written, following Lasaga (1998), as:

$$r(t) = \frac{d\bar{n}_{H_2}}{dt} = r_0 \times \left(1 - \frac{Q_i}{K_i}\right), \qquad (S\text{-}3)$$

with $r_0 = k_0 \times A \times \exp\left(\frac{-E_a}{RT}\right)$. Q_i is computed by assuming that H_2 is an ideal gas and that the activity of $Fe(OH)_2$ in ferroan brucite is equal to its molar fraction ($X_{Fe(OH)_2}$). This leads for Reaction S-1 to $Q_1 = \frac{[H_{2,aq}]}{X_{Fe(OH)_2}{}^3}$ with $[H_{2,aq}] = \frac{n_{H_2}}{V_{aq}}$, and for Reaction S-2 to $Q_2 = \frac{P_{H_2}}{X_{Fe(OH)_2}{}^3}$ with $P_{H_2} = \frac{n_{H_2,g} \times R \times T}{V_g}$. Introducing

Henry's coefficient ($K_H = \frac{P_{H_2}}{[H_2]}$) allows to relate $n_{H_2,g}$ to n_{H_2} as $n_{H_2,g} = \frac{K_H V_g}{K_H V_g + RTV_{aq}} n_{H_2}$. Assuming that V_{aq} and V_g remain constant during the experiment provides the same expression for $\frac{Q_r}{K_r}$ in Reactions S-1 and S-2:

$$\frac{Q_1}{K_1} = \frac{Q_2}{K_2} = \frac{n_{H_2}}{n_{H_2,eq}} \left(\frac{X_{Fe(OH)_2,eq}}{X_{Fe(OH)_2}}\right)^3. \tag{S-4}$$

Combining Equation S-4 with an expression of $X_{Fe(OH)_2}$ derived from mass conservation in Reactions S-1 and S-2 ($X_{Fe(OH)_2} = \frac{n°_{Fe} - 3n_{H_2}}{n°_{Fe} - 3n_{H_2} + n°_{Mg}}$) allows to express $r(t)$ as a function of n_{H_2} only as:

$$r(t) = \frac{d\bar{n}_{H_2}}{dt} = \frac{r_0}{f(n_{H_2}(t))}, \tag{S-5}$$

where $f(n_{H_2}(t)) = \frac{1}{1 - \frac{n_{H_2}(t)}{n_{H_2,eq}} \times \left(\frac{(n°_{Fe} - 3n_{H_2,eq})(n°_{Fe} - 3n_{H_2}(t) + n°_{Mg})}{(n°_{Fe} - 3n_{H_2,eq} + n°_{Mg})(n°_{Fe} - 3n_{H_2}(t))}\right)^3}$.

We measured n_{H_2} by sampling the gas phase either at the end of the experiment (298 K) or *in situ* (experiment SP#6). During all these measurements, the calculated fraction of H_2 in the aqueous phase is below 3 mol % and was thus neglected. The value of n_{H_2} at equilibrium ($n_{H_2,eq}$) was set to the last measurement of H_2 times a factor (λ) slightly above 1 to account for the fact that n_{H_2} asymptotically tends towards the value at the equilibrium according to Reaction S-3. λ was varied between 1.01 and 1.2 to estimate its impact on the derived kinetic constants (Fig. 2). The parameter r_0 was determined by least-square regression of Equation S-5 through the experimental n_{H_2} dataset. The activation energy and the $k_0 \times A$ product were retrieved with a linear fit in a $\ln(r_0)$ *vs.* $1/T$ plot.

Retrieval of $\Delta_f H°$ and $S°$ of the Fe(OH)$_2$ End Member: Calculation Method

For Reactions S-1 and S-2 with H_2 in either the aqueous or gas phase, by definition:

$$\Delta_r G^{P,T} = \left(\sum_i^{phases} v_i \Delta_a H_i^{P,T}\right) - T \times \left(\sum_i^{phases} v_i S_i^{P,T}\right) + RT \ln \prod_i a_i^{v_i}, \tag{S-6}$$

with $\Delta_a H_i^{P,T} = \Delta_f H_i° + \int_{Tr}^{T} Cp_i dT + V_i^0 (P - P_r)$ and $S_i^{P,T} = S_i° + \int_{Tr}^{T} \frac{Cp_i}{T} dT$.

Equation S-6 can be simplified assuming equilibrium conditions, *i.e.* $\Delta_r G^{P,T} = 0$ and $\prod_i a_i^{v_i} = K$ and expressed as a function of two unknowns, $\Delta_f H°_{Fe(OH)_2}$ and $S°_{Fe(OH)_2}$. All the other parameters can be calculated from tabulated data (slop98.dat database and Klein *et al.*, 2009 for other amakinite parameters).

Considering the experimental dataset with all the experiments (j) having reached equilibrium at T_j and P_j, a system of equations is obtained:
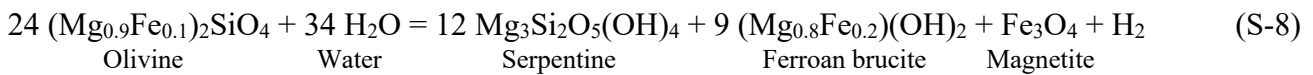
$$\Delta_f H°_{Fe(OH)_2} - T_j \times S°_{Fe(OH)_2} = f_j(T_j, P_j). \tag{S-7}$$

$\Delta_f H°_{Fe(OH)_2}$ and $S°_{Fe(OH)_2}$ values are then determined by least-squares regression (Fig. S-3).

Numerical Modelling of H_2 Production During Serpentinised Dunite Alteration

A numerical model was developed to determine the contribution of both olivine and ferroan brucite to H_2 production during the reaction of a partly serpentinised dunite at 363 K. The initial composition of the serpentinised dunite was determined by assuming that half of the olivine was already serpentinised according to the following reaction (initial serpentinisation degree of 50 %):

$$24 \ (Mg_{0.9}Fe_{0.1})_2SiO_4 + 34 \ H_2O = 12 \ Mg_3Si_2O_5(OH)_4 + 9 \ (Mg_{0.8}Fe_{0.2})(OH)_2 + Fe_3O_4 + H_2 \qquad \text{(S-8)}$$

Olivine   Water   Serpentine   Ferroan brucite   Magnetite

This leads to an initial mineral assemblage with molar fractions in ferroan brucite, olivine, serpentine and magnetite of 20 mol %, 52 mol %, 26 mol % and 2 mol %, respectively.

The production of H_2 during serpentinised dunite alteration at 363 K was considered to depend on three processes: (i) ferroan brucite alteration, (ii) olivine serpentinisation, and (iii) H_2 leakage due to fluid flow or diffusion (also referred to as 'H_2 escape rate' in the main text).

Regarding (i), ferroan brucite was considered to form magnetite according to Reaction 1 at the rate provided in Equation S-3. The value of $n_{H_2,eq}$ required in this latter equation was computed with PHREEQC considering H_2 in equilibrium with an assemblage composed of ferroan brucite + magnetite + chrysotile. The llnl.dat database was used with the thermodynamic data for ferroan brucite derived in the previous section.

Olivine serpentinisation (ii) was modelled according to Reaction S-8. The rate of H_2 production was modelled with the following surface-dependent zero-order rate law:

$$\frac{dn_{H_2,ol}}{dt} = -\left(\frac{1}{24}\right)\frac{\partial n_{ol}}{\partial t} = k_{ol}SAM_{ol}n_{ol}(t). \qquad \text{(S-9)}$$

M_{ol} is the molecular weight of olivine. k_{ol} is calculated as $\frac{k_{MD}}{SA_{MD}}$. One should note that, on the contrary to ferroan brucite alteration rate (Eq. S-3), $n_{H_2,ol}$ does not depend on the total amount of H_2, n_{H_2}. This is consistent with thermodynamic predictions of complete olivine reaction even at high activity in H_2 (*e.g.*, McCollom and Bach, 2009). Ferroan brucite formed during olivine serpentinisation (Reaction S-8) is also added to the amount of ferroan brucite available for H_2 production (ferroan brucite alteration (i)).

H_2 "leakage" (iii) was assumed to be proportional to the H_2 concentration in the fluid expressed as the number of moles of H_2 in the fluid over the mass of water in contact with the rock at each time step:

$$\frac{dn_{H_2,leak}}{dt} = \frac{-n_{H_2}}{m_{water}}J. \qquad \text{(S-10)}$$

J is assumed here to be constant. For the fluid flow case, J corresponds to the rate of water renewal. In this latter case, a cumulative water to rock ratio can be calculated as the integral of J over time. Moreover, fluid flow also induces Mg, Si and Fe transport as aqueous species. The solubility of Mg, Fe and Si in the fluid at the equilibrium with serpentinised dunite were retrieved from the thermodynamic calculation performed with PHREEQC in (i). The predicted pH is 9.7. The solubility in Mg of 6.2×10^{-5} mol/kg at 363 K is approximately 4 and 5 orders of magnitude higher than for Si and Fe, respectively. Ferroan brucite is thus predicted to be the main phase to dissolve during the simulation. The product of Mg solubility by the cumulative water to rock ratio was used to estimate the extent of ferroan brucite dissolution associated with fluid flow.

For the diffusion case, J can be expressed as:

$$J = \frac{D\rho_{\text{water}}A_{\text{h}}}{z}.$$ (S-11)

Combining Equations S-10 and S-11 and assuming $n_{\text{H}_2} = 0$ at the surface ($z = 0$) allow to retrieve Fick's first law of diffusion. A maximum of $\frac{dn_{\text{H}_2,\text{leak}}}{dt}$ for diffusion can be estimated by using $n_{\text{H}_2} = n_{\text{H}_2,\text{eq}}$, D corresponding to H_2 diffusion in bulk water (no tortuosity; 5×10^{-9} m²/s at 298 K), $z = 2500$ m by using a geothermal gradient of 30 K/km, $\rho_{\text{water}} = 1000$ kg/m³ and $A_{\text{h}} = \frac{m_{\text{rock}}}{\rho_{\text{rock}}h}$ with $\rho_{\text{rock}} = 3000$ kg/m³ and $h = 1$ m, the minimum estimated thickness for reacting serpentinised peridotites at depth. With these values, the maximum diffusive flux of H_2 is of 1.3×10^{-15} mol H_2/day/g rock.

Equations S-3, S-9 and S-10 define a system of three differential equations. This system was numerically solved with an adaptive time step depending on the maximum of n_{H_2} variation for each process.

Supplementary Tables

Table S-1   Symbols used.

Symbol	Definition	Units
$X_{\text{Fe(OH)}_2}$	molar fraction of Fe(OH)$_2$ in brucite	–
$X_{\text{Fe(OH)}_2,\text{eq}}$	equilibrium molar fraction of Fe(OH)$_2$ in brucite at T and P	–
x	initial $X_{\text{Fe(OH)}_2}$	–
y	parameter related to reaction progress as defined in Equation 2	–
r	hydrogen (H$_2$) production rate	mol s^{-1}
r_0	hydrogen production rate as defined in Equation S-3	mol s^{-1}
k_0	reaction kinetic constant of ferroan brucite alteration	mol m^{-2} s^{-1}
k_{ol}	reaction kinetic constant of olivine serpentinisation	mol m^{-2} s^{-1}
k_{MD}	maximum reaction constant provided in McCollom and Donaldson (2016) for H$_2$ production during olivine serpentinisation at 363 K	mol kg^{-1} s^{-1}
n_{H_2}	total amount of H$_2$ produced in the experiment	mol
$\bar{n}_{\text{H}_2}$	total amount of H$_2$ produced in the experiment normalised to the mass of starting Fe-brucite material	mol kg^{-1}
$n_{\text{H}_2,\text{g}}$	amount of H$_2$ in the gas phase	mol
$n_{\text{H}_2,\text{eq}}$	equilibrium amount of H$_2$ produced at T and P	mol
$n_{\text{H}_2,\text{ol}}$	amount of H$_2$ produced during Reaction S-8	mol
$n_{\text{H}_2,\text{leak}}$	amount of H$_2$ leaking in the model of serpentinised dunite alteration	mol
n_{ol}	amount of olivine in the serpentinised dunite in the model of serpentinised dunite alteration	mol
m_{water}	mass of water in contact with the rock at each time step of the serpentinised dunite alteration model	kg
m_{rock}	mass of rock in the serpentinised dunite alteration model	kg
λ	factor used to convert last measured n_{H_2} value into $n_{\text{H}_2,\text{eq}}$	–
$n^{\circ}{}_{\text{Fe}}, n^{\circ}{}_{\text{Mg}}$	initial number of moles of Fe and Mg in ferroan brucite	mol
A	ferroan brucite specific surface area	m^2 kg^{-1}
SA_{MD}	surface area of the olivine used in McCollom and Donaldson (2016)	m^2 kg^{-1}
SA	specific surface area of olivine calculated with the relationship provided in Brantley and Melott (2000) for a grain size of 500 μm, typical for serpentinised dunites in ophiolites (Malvoisin *et al.*, 2017)	m^2 kg^{-1}
R	universal gas constant	J mol^{-1} K^{-1}
T	temperature	K
Q_i	quotient of reaction i with i = 1 or 2	–
K_i	equilibrium constant of reaction i with i = 1 or 2	–
E_{a}	activation energy of reaction	J mol^{-1}
P_{H_2}	partial pressure of H$_2$ in the gas phase	bar
$P_{\text{H}_2,\text{eq}}$	partial pressure of H$_2$ in the gas phase at the equilibrium	bar
[H$_2$]	concentration of H$_2$ in the aqueous phase	mol m^{-3}
K_{H}	Henry's coefficient for H$_2$ gas	Pa m^3 mol^{-1}
V_{g}	volume of the gas phase	m^3
V_{aq}	volume of the aqueous phase	m^3
$\Delta_r G^{P,T}$	Gibbs free energy of reaction at T and P	J mol^{-1}
$\Delta_a H_i^{P,T}$	apparent enthalpy of phase i at T and P	J mol^{-1}
$S_i^{P,T}$	third-law entropy of phase i at T and P	J mol^{-1} K^{-1}
$\Delta_f H_i^{\circ}$	standard formation enthalpy of phase i (from the elements)	J mol^{-1}
$\Delta_f G_i^{\circ}$	standard formation Gibbs free energy of phase i	J mol^{-1}
S_i°	standard third-law entropy of phase i	J mol^{-1} K^{-1}
Cp_i	molar heat capacity function of phase i valid in the T_r–T temperature range	J mol^{-1} K^{-1}
V_i^0	molar volume of phase i at reference P_r and T_r	m^3 mol^{-1}
a_i	activity of phase i	–
ν_i	stoichiometric coefficient of phase i	–

Table S-1 continued.

Symbol	Definition	Units
T_r	reference temperature (298 K)	K
P_r	reference pressure (0.1 MPa)	Pa
T_j	temperature at equilibrium for experiment j	K
P_j	pressure at equilibrium for experiment j	Pa
f_j	sum of parameters which can be calculated from tabulated data of Klein *et al.* (2009) in Equation S-6	$\mathrm{J\,mol^{-1}\,K^{-1}}$
J	constant fixing the H_2 escape rate in the model of serpentinised dunite alteration	$\mathrm{kg\,s^{-1}}$
D	diffusion coefficient of H_2 in the fluid	$\mathrm{m^2\,s^{-1}}$
ρ_{water}	water density	$\mathrm{kg\,m^{-3}}$
ρ_{rock}	rock density	$\mathrm{kg\,m^{-3}}$
A_h	area of the horizontal section through which H_2 diffuses	$\mathrm{m^2}$
h	vertical thickness of the serpentinised peridotite layer reacting in the model of serpentinised dunite alteration	m

Table S-2 Experimental conditions for each experiment, produced H_2 and XRD analysis results. Expected H_2 production assuming equilibrium is also calculated with PHREEQC using the thermochemical data retrieved in the present study. f-brc, ferroan brucite; mag, magnetite; pyr, pyroaurite; L/V, liquid-vapor equilibrium; n.d., not detected; n.c., not calculated; thermo., thermodynamic data used for determining thermodynamic parameters of $Fe(OH)_2$; and kin., kinetic data used for determining the kinetic law (predicted duration to reach measured n_{H_2} is not provided for these experiments). * 53.3 ± 16.5 wt. % Fe(III)-bearing brucite (see Carlin *et al.*, 2023) have also been detected in Run caps#t4. Errors are provided as ±3 times the standard deviation.

	Initial experimental conditions						XRD analysis output					PHREEQC	Kinetics	
run name	duration (h)	temperature (K)	initial pressure at T (MPa)	initial f-brc mass (g)	mass water-rock ratio	measured n_{H_2} from GC (mol)	$X_{Fe(OH)_2}$ in initial f-brc (%)	$X_{Fe(OH)_2}$ in final f-brc (%)	final f-brc (wt. %)	mag (wt. %)	pyr (wt. %)	simulated n_{H_2} at equilibrium (mol)	predicted duration to reach measured n_{H_2} (h)	use
caps#1	360	378	20	0.01-0.03	3.33-10	2.87E-09	15.6±2.1	11.0±1.2	93.8±1.2	3.2±0.6	3.3±0.9	1.80E-09	146	thermo.
caps#2	624	378	20	0.032	3.13	8.49E-09	15.6±2.1	12.9±1.8	95.3±1.2	4.7±1.2	n.d.	1.80E-09	267	thermo.
caps#3	984	423	20	0.046	2.17	2.11E-07	18.5±1.8	11.6±0.6	90.8±1.2	9.2±1.2	n.d.	3.07E-08	29	thermo.
caps#4	984	473	20	0.048	2.08	1.29E-06	18.5±1.8	15.8±0.3	92.8±0.6	7.2±0.6	n.d.	3.48E-07	1	thermo.
caps#6	1344	348	20	0.049	2.06	1.91E-10	17.9±2.1	14.7±1.5	89.2±2.1	6.3±1.2	4.5±1.8	5.50E-10	214	thermo.
caps#7	1344	403	20	0.049	2.06	1.91E-09	17.9±2.1	12.9±1.5	90.3±1.5	9.7±1.5	n.d.	1.00E-08	2	thermo.
caps#9	60	378	20	0.040	2.50	1.21E-07	18.1±2.7	13.7±2.1	99.8±0.3	0.2±0.3	n.d.	2.82E-09	2707	not used
caps#10	60	423	20	0.050	2.00	1.75E-07	18.1±2.7	10.2±2.4	97.4±0.9	2.6±0.9	n.d.	2.87E-08	23	thermo.
caps#11bis	60	473	20	0.050	2.00	5.88E-07	18.1±2.7	18.5±0.9	95.1±0.9	4.9±0.9	n.d.	3.27E-07	0.8	thermo.
caps#12bis	60	523	20	0.046	2.17	3.68E-06	18.1±2.7	16.2±0.9	92.6±0.9	8.4±0.9	n.d.	2.65E-06	<0.1	thermo.
caps#13	296	523	20	0.059	1.69	1.42E-06	18.1±2.7	19.8±0.3	92.0±0.9	8.0±0.9	n.d.	2.74E-06	<0.1	thermo.
caps#14	240	573	20	0.025	4.00	5.45E-06	18.1±2.7	12.1±0.6	83.6±1.2	16.4±1.2	n.d.	7.81E-06	<0.1	thermo.
caps#15	48	573	20	0.053	1.89	6.08E-06	18.1±2.7	15.6±0.6	87.3±1.2	12.7±1.2	n.d.	1.14E-05	<0.1	thermo.
SP#3	192	473	1.55 (L/V)	1.52	24.42	1.71E-04	15.6±2.1	20.1±0.3	94.0±0.9	6.0±0.9	n.d.	3.20E-04		kin./thermo.
SP#4	312	473	1.55 (L/V)	0.31	64.52	6.06E-05	18.5±1.8	16.0±0.6	90.7±0.6	9.3±0.6	n.d.	1.85E-04		kin./thermo.
SP#5	408	423	0.476 (L/V)	1.52	24.41	2.45E-05	17.9±2.1	17.7±0.9	93.4±0.9	6.6±0.9	n.d.	1.16E-04		kin./thermo.
SP#6	1656	378	5	1.495	19.80	4.89E-06	18.1±2.7	19.5±1.2	94.9±1.2	3.1±0.6	2.1±0.9	2.81E-05		kin./thermo.

Table S-2 continued.

| run name | Initial experimental conditions | | | | | measured n_{H_2} from GC (mol) | XRD analysis output | | | | | PHREEQC | Kinetics | use |
	duration (h)	temperature (K)	initial pressure at T (MPa)	initial f-brc mass (g)	mass water-rock ratio		$X_{Fe(OH)_2}$ in initial f-brc (%)	$X_{Fe(OH)_2}$ in final f-brc (%)	final f-brc (wt. %)	mag (wt. %)	pyr (wt. %)	simulated n_{H_2} at equilibrium (mol)	predicted duration to reach measured n_{H_2} (h)	
caps#t1	0.5	378	0.121 (L/V)	0.0624	1.60	8.13E-10	20.5±1.8	11.5±1.5	86.6±3	1.6±0.9	11.8±3	4.19E-07		not used
caps#t2	2	378	0.121 (L/V)	0.0639	1.56	5.58E-10	20.5±1.8	14.6±1.5	95.4±1.5	1.5±0.9	3.1±0.9	4.18E-07		not used
caps#t3	143	378	0.121 (L/V)	0.0656	1.52	1.53E-08	20.5±1.8	13.5±1.2	84.8±2.4	2.8±0.9	12.4±2.4	4.17E-07		not used
caps#t4	335	378	0.121 (L/V)	0.0567	1.76	4.62E-10	20.5±1.8	n.c.	39.4±2.1*	3.1±0.9*	18.0±3.9*	4.23E-07		not used
caps#t5	0.5	423	0.476 (L/V)	0.0421	2.38	7.33E-10	20.5±1.8	13.7±1.5	90.2±2.4	1.8±0.9	8.1±2.4	2.65E-06		kin.
caps#t6	72	423	0.476 (L/V)	0.027	3.71	8.79E-09	20.5±1.8	14.6±0.9	98.2±0.6	1.8±0.6	n.d.	2.53E-06		kin.
caps#t7	163	423	0.476 (L/V)	0.0509	1.97	4.93E-08	20.5±1.8	15.4±0.9	97.9±0.6	2.1± 0.6	n.d.	2.67E-06		kin.
caps#t8	483	423	0.476 (L/V)	0.0519	1.93	2.02E-07	20.5±1.8	15.0±0.9	97.6±0.6	2.4±0.6	n.d.	2.67E-06		kin.
caps#t9	721	423	0.476 (L/V)	0.0527	1.90	5.57E-07	20.5±1.8	15.8±0.9	96.9±0.6	3.1±0.6	n.d.	2.68E-06		kin.
caps#t11	1872	423	0.476 (L/V)	0.0557	1.80	1.38E-06	20.5±1.8	20.8±0.3	95.6±0.6	4.4±0.6	n.d.	2.69E-06		kin.
caps#t12	3552	423	0.476 (L/V)	0.0454	2.20	2.33E-06	20.5±1.8	19.7±0.3	94.1±0.9	6.0±0.9	n.d.	2.63E-06		kin./thermo.

Table S-3 Evolution of the number of moles of H_2 (n_{H_2}) measured with gas chromatography as a function of time for SP#6 (378 K, 5 MPa).

duration (h)	measured n_{H_2} from GC (mol)
0	1.12E-07
5	1.44E-07
22	1.80E-07
51	2.31E-07
77	2.53E-07
150	3.24E-07
188	3.63E-07
219	3.41E-07
312	5.17E-07
363	5.22E-07
744	2.76E-06
987	3.55E-06
1078	4.00E-06
1198	4.42E-06
1323	4.58E-06
1390	4.73E-06
1487	4.70E-06

Table S-4 Summary of available $Fe(OH)_2$ thermodynamic data. *a*, *b* and *c* are the coefficients of the equation of Maier and Kelley (1932) for C_p: $C_p = a + bT + cT^{-2}$.

References	$\Delta_f H^\circ$	$\Delta_f G^\circ$	S°	*a*	*b*	*c*
	kJ/mol	kJ/mol	J/mol/K	J/mol/K	(10^3) J/mol/K^2	(10^{-5}) J K/mol
Wagman *et al.* (1982) - NBS	-569.0	-486.5	88.0			
Chase (1998) - NIST-JANAF	-574.045	-491.97	87.864	97.069		
Leussing and Kolthoff (1953)		-492.58				
Refait *et al.* (1999)		-490				
Ziemniak *et al.* (1995)	-583.39	-500.16	84	90		
Sverjensky and Molling (1992)		-494.97				
McCollom and Bach (2009)	-574.61*	-492.58†	88.0‡	109.035	18.192	-22.51
This study	-581.3*	-498.90	86.4	109.035**	18.192**	-22.51**

*: computed from $\Delta_f G^\circ = \Delta_f H^\circ - 298.15 \Delta_f S^\circ$ with the values of $\Delta_f H^\circ$ and S° provided in the table and standard entropies of the elements taken from Helgeson *et al.* (1978).

†: taken from Leussing and Kolthoff (1953).

‡: taken from Wagman *et al.* (1982).

**: taken from McCollom and Bach (2009), calculated as a linear function of brucite, greenalite and chrysotile C_p functions.
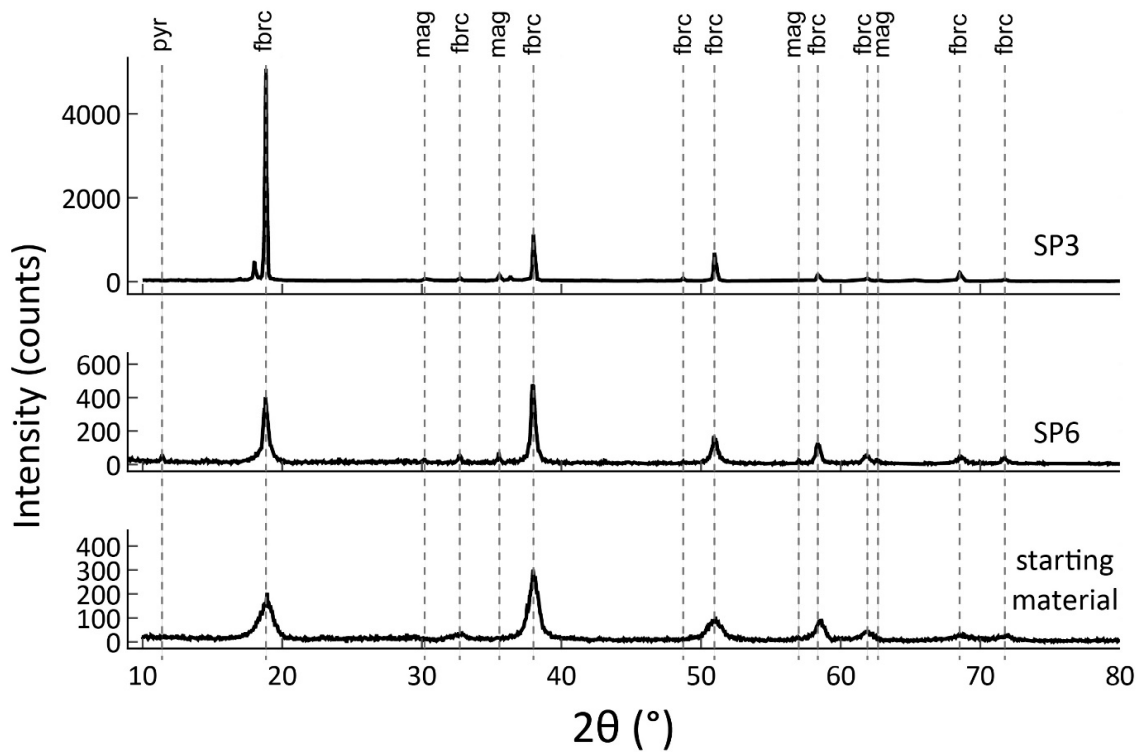
Supplementary Figures

Figure S-1   Selected XRD patterns. From bottom to top: synthetic ferroan brucite starting material, Run SP#6 (378 K, 69 days) and Run SP#3 (473 K, 8 days). fbrc, ferroan brucite; mag, magnetite; pyr, pyroaurite. CuKα radiation.
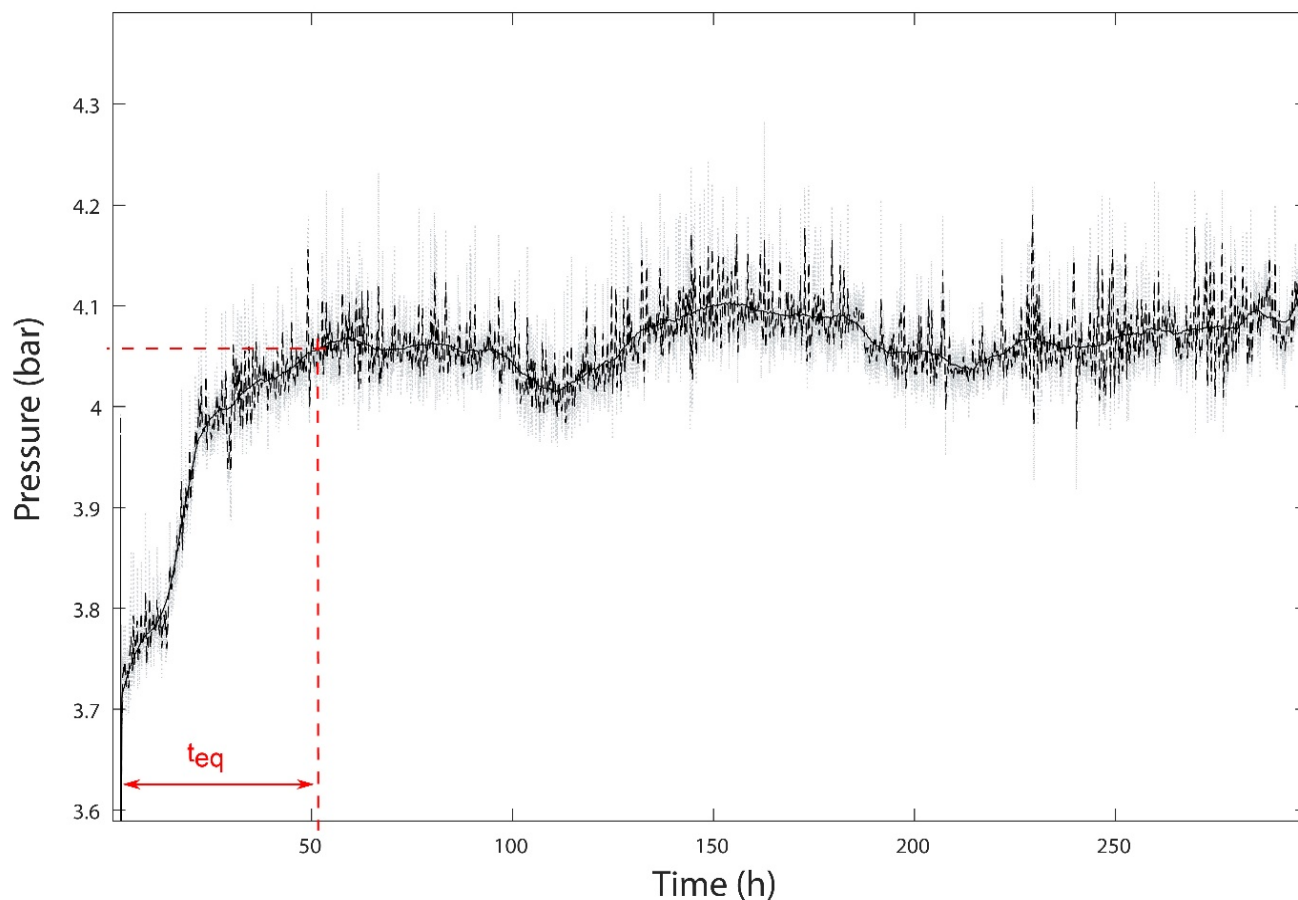
Figure S-2   *In situ* pressure monitoring for SP#5. The grey dotted line, the black dashed line and the solid black curve correspond, respectively, to the raw pressure data, the pressure filtered with a low pass filter, and smoothed filtered pressure. The time to reach equilibrium (t_{eq}; red dashed lines) is graphically determined.
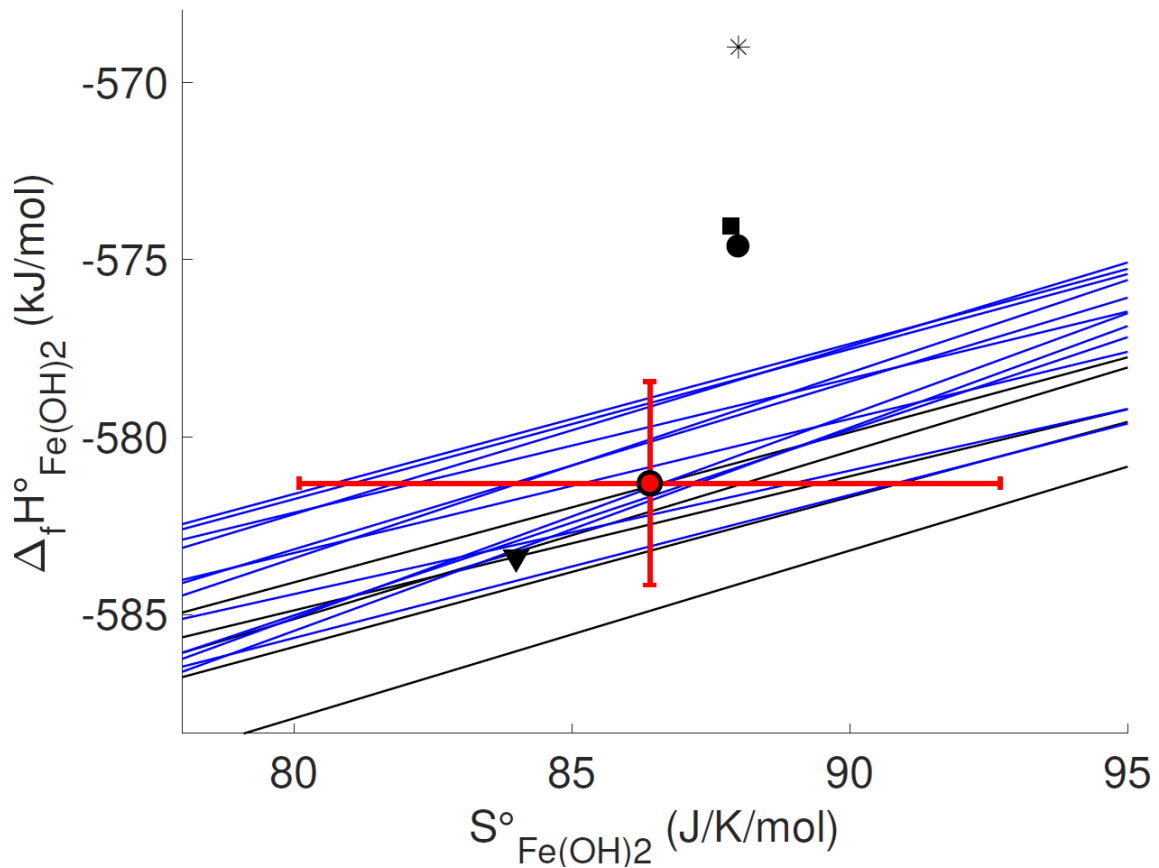
Figure S-3 $\Delta_f H°_{Fe(OH)2}$ *vs.* $S°_{Fe(OH)2}$ relationship determined for capsules experiments (blue lines) and titanium reactor experiments (black lines). The best-fitting $\Delta_f H°_{Fe(OH)2}$ and $S°_{Fe(OH)2}$ values ± their standard error determined by linear regression (R^2 = 0.926) are displayed with a red dot. The black circle, square, triangle and star correspond to the thermodynamic data of McCollom and Bach (2009), Chase (1998), Ziemniak *et al.* (1995) and Wagman *et al.* (1982), respectively.
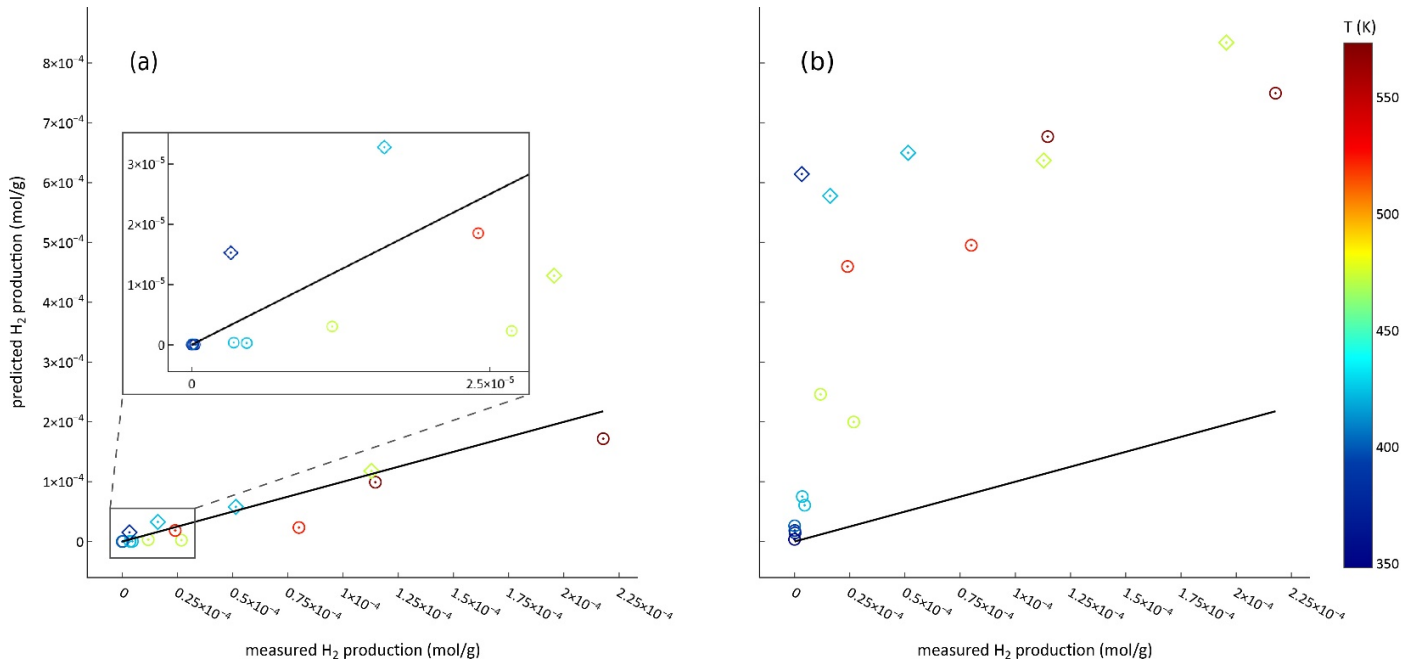
Figure S-4   Measured *vs*. predicted moles of H_2 produced per gram of ferroan brucite in experiments SP#3 to #6 and caps#t12 (diamond symbols), and caps#1 to #15 (circle symbols). The predicted amount of H_2 is equal to the measured amount of H_2 on the black solid line. The predictions were calculated with PHREEQC using the thermodynamic data for $Fe(OH)_2$ **(a)** derived here and **(b)** from Klein *et al.* (2009).

Supplementary Information References

Brantley, S.L., Mellott, N.P. (2000) Surface area and porosity of primary silicate minerals. *American Mineralogist* 85, 1767–1783. https://doi.org/10.2138/am-2000-11-1220

Carlin, W., Malvoisin, B., Lanson, B., Brunet, F., Findling, N., Lanson, M., Magnin, V., Fargetton, T., Jeannin, L., Lhote, O. (2023) Fe^{III}-substituted brucite: Hydrothermal synthesis from ($Mg_{0.8}Fe^{II}_{0.2}$)-brucite, crystal chemistry and relevance to the alteration of ultramafic rocks. *Applied Clay Science* 234, 106845. https://doi.org/10.1016/j.clay.2023.106845

Chase, M.W. (1998) *NIST-JANAF Thermochemical Tables*. Fourth Edition, American Chemical Society, Washington, DC.

Doebelin, N., Kleeberg, R. (2015) *Profex* : a graphical user interface for the Rietveld refinement program *BGMN*. *Journal of Applied Crystallography* 48, 1573–1580. https://doi.org/10.1107/S1600576715014685

Helgeson, H.C., Delany, J.M., Nesbitt, H.W., Bird, D.K. (1978) Summary and critique of the thermodynamic properties of rock-forming minerals. *American Journal of Science* 278-A, 1–229.

Klein, F., Bach, W., Jöns, N., McCollom, T., Moskowitz, B., Berquó, T. (2009) Iron partitioning and hydrogen generation during serpentinization of abyssal peridotites from 15°N on the Mid-Atlantic Ridge. *Geochimica et Cosmochimica Acta* 73, 6868–6893. https://doi.org/10.1016/j.gca.2009.08.021

Lasaga, A.C. (1998) *Kinetic Theory in the Earth Sciences.* Princeton University Press, Princeton, NJ.

Leussing, D.L., Kolthoff, I.M. (1953) The Solubility Product of Ferrous Hydroxide and the Ionization of the Aquo-Ferrous Ion. *Journal of the American Chemical Society* 75, 2476–2479. https://doi.org/10.1021/ja01106a058

Maier, C.G., Kelley, K.K. (1932) An Equation for the Representation of High-Temperature Heat Content Data. *Journal of the American Chemical Society* 54, 3243–3246. https://doi.org/10.1021/ja01347a029

Malvoisin, B., Brunet, F., Carlut, J., Montes-Hernandez, G., Findling, N., Lanson, M., Vidal, O., Bottero, J.-Y., Goffé, B. (2013) High-purity hydrogen gas from the reaction between BOF steel slag and water in the 473–673 K range. *International Journal of Hydrogen Energy* 38, 7382–7393. https://doi.org/10.1016/j.ijhydene.2013.03.163

Malvoisin, B., Brantut, N., Kaczmarek, M.-A. (2017) Control of serpentinisation rate by reaction-induced cracking. *Earth and Planetary Science Letters* 476, 143–152. https://doi.org/10.1016/j.epsl.2017.07.042

McCollom, T.M., Bach, W. (2009) Thermodynamic constraints on hydrogen generation during serpentinization of ultramafic rocks. *Geochimica et Cosmochimica Acta* 73, 856–875. https://doi.org/10.1016/j.gca.2008.10.032

McCollom, T.M., Donaldson, C. (2016) Generation of Hydrogen and Methane during Experimental Low-Temperature Reaction of Ultramafic Rocks with Water. *Astrobiology* 16, 389–406. https://doi.org/10.1089/ast.2015.1382

Refait, Ph., Bon, C., Simon, L., Bourrié, G., Trolard, F., Bessière, J., Génin, J.-M.R. (1999) Chemical composition and Gibbs standard free energy of formation of Fe(II)-Fe(III) hydroxysulphate green rust and Fe(II) hydroxide. *Clay Minerals* 34, 499–510. https://doi.org/10.1180/000985599546280

Sverjensky, D.A., Molling, P.A. (1992) A linear free energy relationship for crystalline solids and aqueous ions. *Nature* 356, 231–234. https://doi.org/10.1038/356231a0

Wagman, D.D., Evans, W.H., Parker, V.B., Schumm, R.H., Halow, I., Bailey, S.M., Chruney, K.L., Nuttall, R.L. (1982) The NBS tables of chemical thermodynamic properties: Selected values for inorganic and C_1 and C_2 organic substances and SI units. *Journal of Physical and Chemical Reference Data* 11, Suppl. 2, 1–392. https://srd.nist.gov/JPCRD/jpcrdS2Vol11.pdf

Ziemniak, S.E., Jones, M.E., Combs, K.E.S. (1995) Magnetite solubility and phase stability in alkaline media at elevated temperatures. *Journal of Solution Chemistry* 24, 837–877. https://doi.org/10.1007/BF00973442